Breaking the bandwidth limit of a high-quality-factor ring modulator based on thin-film lithium niobate

Yu Xue
Zhejiang University
Ranfeng Gan
South China Normal University
Kaixuan Chen
South China Normal University
Gengxin Chen
Zhejiang University
Ziliang Ruan
Zhejiang University
Junwei Zhang
Sun Yat-Sen University
Jie Liu
Sun Yat-sen University
Daoxin Dai
Zhejiang University
Changjian Guo
South China Normal University
Liu Liu (liuliuopt@zju.edu.cn)
Zhejiang University https://orcid.org/0000-0002-4927-9562

Article

Keywords:

Posted Date: July 5th, 2022

DOI: https://doi.org/10.21203/rs.3.rs-1816496/v1

Abstract

Growing global data traffic requires high-performance modulators with a compact size, a large bandwidth, a low optical loss, and a small power consumption. A careful trade-off among these parameters usually has to be made when designing such a device. Here, we propose and demonstrate an electro-optic ring modulator on the thin-film lithium niobate platform without compromising between any performances. The device exhibits a low on-chip loss of about -0.15dB with a high intrinsic Q-factor of 7.7×10^5. Since a pure coupling modulation is employed, the photon life-time is no longer a limiting factor for the modulation speed. A large electro-optic bandwidth is obtained without any roll-off up to 67 GHz. The device, with a footprint of 3.4 mm×0.7 mm, also exhibits a low half-wave voltage of 1.75 V, corresponding to a half-wave voltage length product of 0.35 V•cm considering the 2-mm long modulation section. Driverless data transmission up to 240 Gb/s is also demonstrated.

Full Text

Light modulation is a key function required in many optical applications, such as optical interconnect[1,2], optical computing[3], microwave photonics[4], laser detection and ranging[5,6]. A modulator simultaneously with a compact size, a large modulation bandwidth, a low insertion loss, a high extinction ratio, a low driving voltage, and a wide working wavelength range is always desired, and many research efforts for it has been made during the last decades. To address the above performance metrics, a variety of material platforms and device structures has been introduced. Semiconductor-based optical modulators on Si or InP, for example, can usually present a large modulation efficiency, which leads to a small device footprint[7-9]. Their matured micro-fabrication processes in wafer scales further enable the integration of them in complex photonic circuits[10,11]. However, being a semiconductor device, the operational speed of such modulators is still limited, to some extent, by the carrier dynamics[12]. For example, Si-based modulators with buried PN junctions still exhibit modulation bandwidths up to several tens of GHz[13,14]. They often suffer from a high insertion loss due to optical absorptions resulted from the carriers[12,15]. Alternatively, electro-optical (EO) material exhibiting a linear Pockels effect can be used to construct a high-performance modulator potentially[16]. Pockels effect, resulted from the variation of the spontaneous electric polarization by an external electric field, is nearly instantaneous[17]. Therefore, it can support light modulation at a very high speed. However, such an effect can only be presented in non-centrosymmetric crystals or engineered composite materials, such as, lithium niobate (LN)[18], barium titanate[19], lead zirconate titanate[20], and polymers[21]. Among them, LN is probably the best-known EO material, which has a Pockels coefficient of ~30 pm/V[18]. Currently LN has been widely and successfully adopted in commercial modulator products for decades due to its excellent properties of wide transparent wavelength window, ultra-low optical loss, and high stability[18], even though some other materials with a very high Pockels coefficient do exist[19-21]. Yet, conventional LN modulators remain bulky and discrete suffered from the low refractive index contrast of a diffusion-based waveguide structure[22]. Recently, thin-film LN (TFLN) emerges as a promising platform for integrated photonic devices using LN[23-27]. The

etched submicron-sized waveguide on TFLN offers a high refractive index contrast, which leads to demonstrations of EO modulators with footprints shrunk to about one tenth of the conventional ones in bulk LN. The driving voltage of such TFLN-based modulators has also been reduced to <1V, and then can be delivered directly through a CMOS (complementary metal-oxide-semiconductor) circuit without using any microwave amplifier[25, 27]. Therefore, the energy consumption of the whole signal transmitter can be largely decreased.

Despite its great success, a TFLN modulator based on a classic Mach-Zehnder interferometer (MZI) structure is still large usually with a length of several centimeters[27]. To further reduce the size of a modulator, resonant structures can be employed, including Fabry-Pérot cavities[28,29], photonic crystal cavities[30], or micro-rings[31]. For example, Si-based ring modulators have already been presented with lowered insertion losses, shrunk footprints, and comparable modulation bandwidths when compared to MZI modulators[32]. The conventional working principle of a resonant modulator relies on the shift of its resonance by an external electrical stimulation[7]. In this way, the transmitted light near the resonant wavelength can be modulated. The quality-factor (Q-factor) of such a resonator is the key parameter for modulation. On one hand, increasing the Q-factor can effectively reduce the driving voltage due to the relatively small resonant shift required to achieve sufficient modulation depth. On the other hand, a high-Q resonator would largely decrease the modulation speed due to the elongated photon lifetime inside the resonator[33,34]. To release this compromise, a strategy of coupling modulation has been proposed[34]. By modulating the coupling strength of the resonator to the bus waveguide, the light transmission can also be modulated while maintaining the resonant wavelength unchanged in theory. In this way, the time-consuming photon rebuilding in a high-Q resonator can be avoided. A resonant modulator simultaneously with a low driving voltage and a large modulation bandwidth can therefore be expected. Unfortunately, this is not achieved experimentally yet. Preliminary demonstrations of such a coupling modulation in ring resonators on Si did not show significant improvements on performances as compared to the conventional modulation scheme[35,36]. This is mainly due to two facts. First, an ultra-high-Q ring is difficult to achieve on Si especially when a PN junction for modulation is embed. Second, it is also difficult to achieve a pure coupling modulation without affecting the resonant wavelength when using the free-carrier effect in Si.

In this paper, we report, for the first time, a high Q-factor ring modulator on TFLN with an ultra-high speed and low driving voltage by utilizing a pure coupling modulation. An MZI structure working in a push-pull configuration is employed as the modulated coupler of a ring resonator, whose measured intrinsic Q-factor reaches 7.7×10^5. An effective half-wave voltage V_π of 1.75 V is obtained, corresponding to a record-low half-wave-voltage-length product $V_\pi L$ of 0.35 V•cm considering the TFLN MZI structure. The device also presents a flat modulation frequency response without any noticeable roll-off up to 67 GHz, which breaks the photon-lifetime limit in a typical resonant modulator. As an example application, driverless data transmission up to 240 Gb/s, using 4-level pulse-amplitude modulation (PAM-4) format, is also demonstrated. Moreover, the device footprint is only about 3.4 mm×0.7 mm, which is significantly smaller than other high-speed and low-driving-voltage TFLN modulators.

Structure and principle

The structure of the proposed ring modulator is shown in Fig. 1a, which consists of a standard 2×2 MZI modulator structure and a loop waveguide connecting two ports of the MZI. The other two ports are considered as the light input and output ports of the present modulator. This structure is essentially a ring resonator with an MZI to tune the coupling ratio between the ring and the bus waveguide. Clearly, the key part of this design is the MZI coupling-ratio modulator. Here, a periodic capacitively-loaded traveling-wave (CLTW) electrode structure is adopted, which has been proved to give so far the best modulation performances on TFLN[37-39]. The whole device structure is designed and fabricated on a commercial x-cut LN-on-insulator (LNOI) wafer with a 400-nm thick TFLN layer and a 3-μm thick buried oxide layer on a Si substrate (see Methods). Grating couplers are used as fiber-to-chip interfaces[40]. Pictures of a finished sample is illustrated in Fig. 1b - 1d.

The working principle of the present device can be described as follows. First, the transmission of the MZI is initially set to ensure that the ring resonator is working at a critical-coupled state (Fig. 1e). In this case, the transmission of the whole device should be zero theoretically at the resonant wavelength. Then, the MZI is tuned to a state that the coupling to the cross port is zero, i.e., zero-coupled state (Fig. 1f). Therefore, the light in the bus waveguide is isolated from that circulating in the ring, and the transmission would be high. The ring resonator is designed with a high Q-factor, so that the photon lifetime in the resonator is long at the zero-coupling state. Furthermore, the MZI modulator is designed to work in a push-pull configuration, i.e., the induced phase changes in the two arms have opposite signs. This ensures that during the tuning process only the amplitude of the MZI transmission varies while its phase maintains. Thus, the resonant wavelength of the ring stays unchanged, and the resonant photons built up already in the ring would also be kept. Once the MZI is tuned back, the critical-coupled state can be immediately restored, and the transmission of the device drops. Since the coupling ratio required for a high Q-factor resonator to achieve the critical coupling is small. Therefore, for the operations discussed above, the transmission of the MZI at the crossing port only has to be tuned in a small range to achieve a full modulation depth. The driving voltage of the present device can then be much smaller than that of a conventional MZI modulator. The static wavelength response of the fabricated modulator device was first measured as shown in Fig. 2 (see Methods), where the responses of the GCs are normalized out. The obtained spectrum can be viewed as a ring response with its coupling ratio superimposed onto an MZI response. The free spectrum ranges (FSRs) of the ring and the MZI responses are 0.14 nm and 17.40 nm, respectively. They are also matched well with the simulation results (see Supplementary Note 1). Three regions can be distinguished in this spectrum, i.e., the over-coupled region, the critical-coupled region, and the under-coupled region. Unlike traditional MZI modulators, one has to shift the spectrum for at least half an FSR, so called the half-wave voltage V_{π}, to achieve the largest modulation. Yet, in the present device, a shift from the under-coupled region to the critical-coupled region is enough to ensure the same modulation depth. Figure 2b shows a zoom-in view of the transmission spectrum around the under-coupled region, where the rest of the tests were carried out. Thanks to the compact size, the on-chip insertion losses of the device at non-resonant wavelengths are about -0.15 dB. The intrinsic Q-factor of

the resonances can be deducted as about 7.7×10^5, which is lower than the state-of-the-art result for a ring resonator on TFLN. Nevertheless, it is still orders-of-magnitude higher than those in conventional resonant modulators.

To show the EO modulation properties of the present device, we applied different direct-current (DC) voltages to the device, and monitored the transmission spectrum at one resonant wavelength around 1536.8943 nm. As shown in Fig. 3a, the depth of resonant dip changes according to the applied voltage, while its position is hardly affected, which confirms clearly that the pure coupling modulation is achieved here. Figure 3b shows the dependence of the dip transmissions on the applied voltages. A static extinction ratio (ER) of >20 dB can be obtained. To eliminate any unwanted low-frequency effects of the LN material, the transmission at the resonant wavelength is further recorded using a 100-kHz triangular voltage sweep. We then define an effective V_π of the present device as the voltage swing needed for the maximal modulation depth, which is 1.75 V as shown in Fig. 4. Considering the length of the MZI structure, i.e., 2 mm, a $V_\pi L$ of 0.35 V·cm is obtained, which is also close to the simulation results (see Supplementary Note 2), and considerably less than those achieved in conventional MZI modulators based on TFLN[25-27, 37-39].

High-speed modulation performances.

To demonstrate the high-speed operation of the present modulator as discussed in the previous section, the small signal EO response was then measured, and the results are shown in Fig. 5. The input light here was tuned at one resonant wavelength, 1536.7498 nm, at the under-coupled region. A flat frequency response was presented without a noticeable roll-off up to 67 GHz, which is the measurement limit of our equipment. It is clearly that the measured modulation bandwidth exceeds the photon-lifetime limit of such a high Q-factor modulator, thanks to the coupling modulation scheme. Generally, the measured EO response curve here is matched well to the simulation results (see Supplementary Note 3). The small peaks around multiples of 18.43 GHz is related to the FSRs of the ring resonant response, which can also be predicted in theory[34].

Since the present modulator exhibits a low V_π, it is possible to drive it using direct outputs from CMOS circuits without a microwave amplifier. This can dramatically improve the system performances and reduce the power consumption. To further verify this driverless operation, we performed high-speed data transmissions using the device (see Methods). The experimental setups for measuring eye diagrams and back-to-back bit-error rates (BERs) are shown in Fig. 6a. The raw transmitted eye diagrams of a 160 Gb/s on-off key (OOK) signal and an 80 Gb/s PAM-4 signal using a drive of peak-to-peak voltage V_{pp} = 0.75 V are shown in Figs. 6b and 6c. The dynamic ERs here reach 5 dB. A clear eye-opening can be observed in both cases. Apparently, the resonant peaks in the EO frequency response curves shown in Fig. 5 would not affect the data transmission performances. At higher data rates, the BERs were further calculated off-line using simple feed-forward equalizer (FFE) based linear digital signal process (DSP) algorithms with 200 taps. Figure 6d shows the measured BERs of 200 Gb/s OOK and 160 Gb/s, 224 Gb/s, 240 Gb/s PAM-4 signals at different received light powers just before detection. One can find that the BERs can drop

below the hard-decision forward-error-coding (HD-FEC) threshold (3.8×10^{-3}) up to 224 Gb/s PAM-4 data rate. For the highest measured date rate of 240 Gb/s PAM-4 signal, the BER can drop below the soft-decision forward-error-coding (SD-FEC) threshold (2×10^{-2}), and approach the HD-FEC threshold.

Discussion

Table 1 summarizes performances of some demonstrated intensity modulators on Si and TFLN, including the present ring modulator using the coupling modulation. Thanks to the ring resonator here, the $V_\pi L$ of an MZI structure on the TFLN platform has been pushed almost an-order-of-magnitude lower. This further helps reduce the device length to about 2 mm, while still maintaining a driverless operation. The footprint of such a high-performance TFLN modulator is now at the same level of conventional Si-based MZI modulators. Moreover, the modulation bandwidth of the present resonant modulator is not limited by its Q-factor. It solely depends on that of the 2-mm long MZI structure for modulating the coupling ratio, which can theoretically support a 3-dB EO bandwidth up to 40 THz (see Supplementary Note 3) due to the short length and the advanced CLTW electrodes. This is, to the best of our knowledge, the highest bandwidth among EO modulators in different platforms.

The breaking of the photon life-time limit also means that the device footprint or its effective V_π can be further decreased by improving the intrinsic Q-factor of the ring. As a Q-factor up to 1.14×10^7 has already been demonstrated for a ring on the TFLN platform through optimizing the fabrication processing[41], a V_π of about 0.47 V, i.e., a $V_\pi L$ of 0.094 V•cm, can then be expected for the present device configuration and dimensions (see Supplementary Note 2). Another improvement for the device is to increase its working wavelength range. For better presentation of the device working principle, an MZI structure with unbalanced arm lengths were adopted here as shown in Fig. 1a. The under-coupled region is therefore limited to several nm wavelength range. If a balanced MZI with a separate DC electrode to tune the working point was to be used, the FSR of the MZI response, as well as the working wavelength range, could be largely expanded. The resonant wavelength of the ring response can also be adjusted using another DC electrode on the ring. Since the FSR of the ring is relatively small, a small tuning on the ring resonance is enough to address all the wavelengths between one FSR (see Supplementary Note 4).

In summary, we have introduced a TFLN-based modulator with a compact size of about 3.4 mm×0.7 mm, a large modulation bandwidth reaching in principle THz, a low insertion loss of about -0.15dB, a high static extinction ratio of > 20 dB, and a low driving voltage of 0.75 V. The pure coupling modulation using an MZI and a ring structure facilitates these high performances. With this design, we are able to break the bandwidth limit of a high Q-factor resonant modulator. The demonstrated device here paves the way for realizing a compact EO modulator on the TFLN platform while not compromising between modulation performances. This is important for future high-density integrated circuits with large number of channels in data communications and microwave photonics.

Method

Device fabrication. The fabrication processing of the device starts with the TFLN structure patterning on a commercial x-cut LNOI wafer with a Si substrate (NanoLN) using electron-beam lithography and dry etching. Then, an oxide over-cladding was deposited using plasma enhanced chemical vapor deposition. Two Au layers for the metal electrodes were subsequently deposited using electron beam evaporation and lift-off processes. Finally, holes were etched between the metal electrodes through the over-cladding and buried oxide layers, and the Si substrate was removed beneath the TFLN waveguide at the modulation sections using isotropic Si dry etching. Further details of this process are discussed in ref. [27].

Data transmission measurement. As show in Fig. 6a, a tunable laser source of about 0 dBm output power was used as the light input. The polarization was tuned to transverse electrical mode with a polarization controller (PC). The electrical data signal was generated by a 256-GS/s arbitrary wave generator (AWG) of 70-GHz analog bandwidth (Keysight M8199A), and fed to the device under test (DUT) with a microwave probe (GGB 67A). Another microwave probe was used to provide the 50 W termination. Gray-coded PAM-4 symbols were generated offline using a 2^{19} uniformly distributed pseudorandom sequence. A simple zero-order hold filter with 2 samples per symbol was used for pulse shaping. The sampling rate of the AWG was set to 224 Gsa/s and 240 Gsa/s for generation of 112 Gbaud and 120 Gbaud PAM-4 signals, respectively. For generation of the 200 Gbaud OOK signal, 1 sample per symbol was used. The DUT was fixed on a temperature controlled (TC) stage with its temperature fixed at 25 ^{o}C. The output modulated light was amplified by an erbium-doped fiber amplifier (EDFA) and filtered by a bandpass filter (BPF). It was finally detected by a high-speed photodiode (PD) of 70-GHz bandwidth (Finisar XPDV3120). The electrical signal was recorded using a sampling oscilloscope (SO) of 80-GHz bandwidth (Agilent 86100D) for raw eye-diagram measurements, or a real-time oscilloscope (RO) of 59-GHz bandwidth and 160-GS/s sampling rate (Labmaster 10 Zi-A) for the offline DSP.

References

1. David, A. B. M. Attojoule Optoelectronics for Low-Energy Information Processing and Communications. J. Lightwave Technol. **35**, 346–396 (2017).
2. Sun, C. *et al.* Single-chip microprocessor that communicates directly using light. Nature **528**, 534–538 (2015).
3. Zhou, T. *et al.* Large-scale neuromorphic optoelectronic computing with a reconfigurable diffractive processing unit. Nat. Photonics **15**, 367–373 (2021).
4. Marpaung, D., Yao, J. & Capmany, J. Integrated microwave photonics. Nat. Photonics **13**, 80–90 (2019).
5. Behroozpour, B. *et al.* Lidar system architectures and circuits. IEEE Commun. Mag. **55**, 135–142 (2017).
6. Qian, R. *et al.* Video-rate high-precision time-frequency multiplexed 3D coherent ranging. Nat. Commun. **13**, 1476–1485 (2022).
7. Xu, Q. *et al.* Micrometre-scale silicon electro-optic modulator. Nature **435**, 325–327 (2005).

8. Estaran, J. M. *et al.* 140/180/204-Gbaud OOK Transceiver for Inter- and Intra-Data Center Connectivity. J. Lightwave Technol. **37**, 178–187 (2019).
9. Ogiso, Y. *et al.* 80-GHz Bandwidth and 1.5-V V_{π} InP-Based IQ Modulator. J. Lightwave Technol. **38**, 249–255 (2020).
10. Vladimir S. *et al.* Monolithic silicon-photonic platforms in state-of-the-art CMOS SOI processes. Opt. Express **26**, 13106–13121 (2018).
11. Fu, X. *et al.* 5 x 20 Gb/s heterogeneously integrated III-V on silicon electro-absorption modulator array with arrayed waveguide grating multiplexer. Opt. Express **23**, 18686–18693 (2015).
12. Soref, R. A. & Bennett, B. R. Electrooptical Effects in Silicon. IEEE J. Quantum Electron. **23**, 123–129 (1987).
13. Li, M. F. *et al.* Silicon intensity Mach–Zehnder modulator for single lane 100 Gb/s applications. Photonics Res. **6**, 109–116 (2018).
14. Alam, M. S. *et al.* Net 220 Gbps/λ IM/DD Transmission in O-Band and C-Band With Silicon Photonic Traveling-Wave MZM. J. Lightwave Technol. **39**, 4270–4278 (2021).
15. Hsu, W. C. *et al.* MOS Capacitor-Driven Silicon Modulators: A Mini Review and Comparative Analysis of Modulation Efficiency and Optical Loss. IEEE J. Sel. Top. Quantum Electron. **28**, 1–11 (2022).
16. Thomaschewski M. & Bozhevolnyi S. I. Pockels modulation in integrated nanophotonics. Appl. Phys. Rev. **9**, 021311–021323 (2022)
17. Sun S. S. & Dalton L. R. Introduction to Organic Electronic and Optoelectronic Materials and Devices (CRC Press, 2008).
18. Wooten, E. L. *et al.* A review of lithium niobate modulators for fiber-optic communications systems. IEEE J. Sel. Top. Quantum Electron. **6**, 69–82 (2000).
19. Abel, S. *et al.* Large Pockels effect in micro-and nanostructured barium titanate integrated on silicon. Nat. Mater. **18**, 42–48 (2019).
20. Alexander, K. *et al.* Nanophotonic Pockels modulators on a silicon nitride platform. Nat. Commun. **9**, 1–6 (2018).
21. Haffner, C. *et al.* Low-loss plasmon-assisted electro-optic modulator. Nature **556**, 483–486 (2018).
22. Janner, D. *et al.* Micro-structured integrated electro-optic $LiNbO_3$ modulators. Laser Photonics Rev. **3**, 301–313 (2009).
23. Rao, A. & Fathpour, S. Compact Lithium Niobate Electrooptic Modulators. IEEE J. Sel. Top. Quantum Electron. **24**, 3400114 (2018).
24. Andreas B. *et al.* Status and Potential of Lithium Niobate on Insulator (LNOI) for Photonic Integrated Circuits. Laser Photonics Rev. **12**, 1700256 (2018).
25. Wang, C. *et al.* Integrated lithium niobate electro-optic modulators operating at CMOS-compatible voltages. Nature **562**, 101–104 (2018).
26. He, M. *et al.* High-performance hybrid silicon and lithium niobate Mach–Zehnder modulators for 100 Gbit s^{-1} and beyond. Nat. Photonics **13**, 359–364 (2019).

27. Chen, G. *et al.* Compact 100GBaud driverless thin-film lithium niobate modulator on a silicon substrate. Opt. Express **30**, 25308–25317 (2022).
28. Xu, M. *et al.* Integrated thin film lithium niobate Fabry–Perot modulator. Chin. Opt. Lett. **19**, 060003 (2021).
29. Pan, B. *et al.* Compact Electro-Optic Modulator on Lithium Niobate. Photonics Res. **10**, 697–702, (2022).
30. Li, M. *et al.* Lithium niobate photonic-crystal electro-optic modulator. Nat. Commun. **11**, 4123 (2020).
31. Wang, C. *et al.* Nanophotonic lithium niobate electro-optic modulators. Opt. Express **26**, 1547–1555 (2018).
32. Zhang, Y. *et al.* 240 Gb/s optical transmission based on an ultrafast silicon microring modulator. Photonics Res. **10**, 1127–1133 (2022).
33. Hui, Y. *et al.* Trade-off between optical modulation amplitude and modulation bandwidth of silicon micro-ring modulators. Opt. Express **22**, 15178–15189 (2014).
34. Sacher, W. D. & Poon, J. K. Dynamics of microring resonator modulators. Opt. Express. **16**, 15741–15753 (2008).
35. Sacher, W.D. *et al.* Coupling modulation of microrings at rates beyond the linewidth limit. Opt. Express. **21**, 9722–9733 (2013).
36. Yang, R. *et al.* Low-voltage high-speed coupling modulation in silicon racetrack ring resonators. Opt. Express. **23**, 28993–29003 (2016).
37. Xu, M. *et al.* Dual-polarization thin-film lithium niobate in-phase quadrature modulators for terabit-per-second transmission. Optica **9**, 61–62 (2022).
38. Kharel, P. *et al.* Breaking voltage–bandwidth limits in integrated lithium niobate modulators using micro-structured electrodes. Optica **8**, 357–363 (2021).
39. Chen, G. *et al.* High performance thin-film lithium niobite modulator on a silicon substrate using periodic capacitively loaded traveling-wave electrode. APL Photon. **7**, 026103 (2022).
40. Ruan, Z. *et al.* Metal based grating coupler on a thin-film lithium niobate waveguide. Opt. Express **28**, 35615–35621 (2020).
41. Wu, R. *et al.* Long Low-Loss-Litium Niobate on Insulator Waveguides with Sub-Nanometer Surface Roughness. Nanomaterials (Basel) **8**, 910 (2018).

Declarations

Acknowledgements:

This work is partially supported by National Research and Development Program (2019YFB2203200), National Natural Science Foundation of China (NSFC) (62135012, 62105107, 91950205, 92150302), Leading Innovative and Entrepreneur Team Introduction Program of Zhejiang (2021R01001), Guangdong

Basic and Applied Basic Research Foundation (2021A1515012215, 2021B1515120057), The Fundamental Research Funds for the Central Universities (2021QNA5001).

Author contributions:

L.L. conceived the idea and supervised the project. C.G., J.L., and D.D. provided assistances in the coordination of the project. Y.X. and G.C. designed the device parameters and the layout structure. Y.X., Z.R., and K.C. fabricated the device. Y.X. performed the static measurement and data analyses. R.G., K.C., and J.Z. performed the high-speed and data-transmission measurements. Y.X. and L.L. wrote the manuscript. All the authors reviewed the manuscript and agreed on the contents.

Data availability:

All data that support the findings of this study are available from the corresponding authors upon reasonable request.

Competing interests:

The authors declare that they have no competing financial interests.

Tables

Table 1 | Comparison of several performance metrics for intensity modulators.

atform	Type	Loss (dB)	$V_{\pi}L$ (Vcm)	V_{pp} (V)	EO S_{21} roll-off	Length (mm)	Data rate (Gb/s)
Si[13]	MZI	-5.4	1.4	5	-3 dB @ 55 GHz	2	112 (HD-FEC)
Si[14]	MZI	-5.4	1.35	2.3	-3 dB @ 47 GHz	2.5	225 (SD-FEC)
Si[32]	ring	-1.5	0.8	3	>60 GHz	0.008	240 (SD-FEC)
FLN[38]	MZI	1.5	2.6	/	-1.8 dB @ 50 GHz	20	/
FLN[30]	PC	-2.2	/	2.5	-3 dB @ 17.5 GHz	0.03	11
FLN[39]	MZI	-0.2	2.2	1	-1.4 dB @ 67 GHz	10	112 (KP4-FEC)
This work	ring+MZI	-0.15	0.35	0.75	~0 dB @ 67 GHz -3 dB @ 40 THz (sim.)	2	224 (HD-FEC) 240 (SD-FEC)

Figures

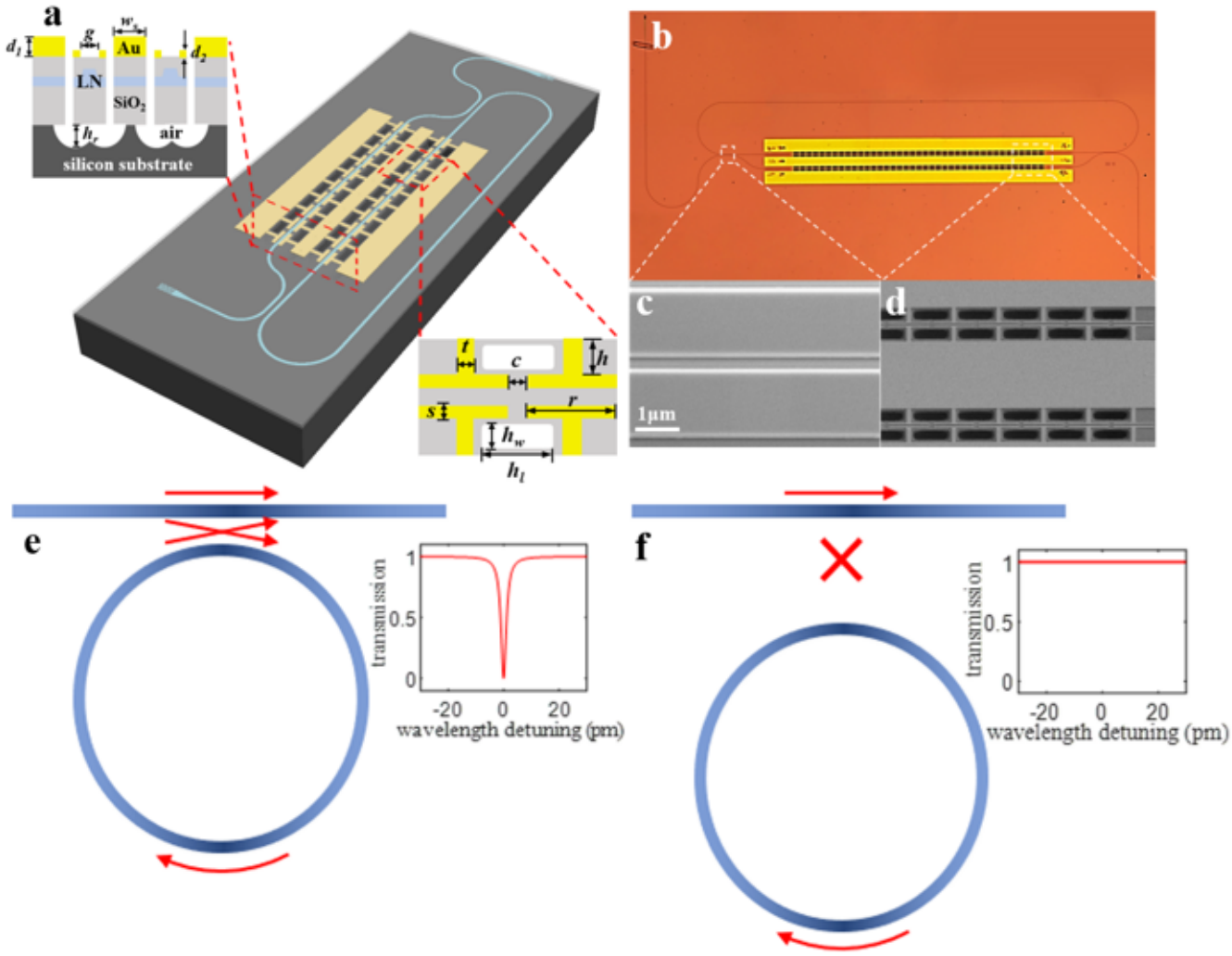

Figure 1

Structure and working principle of the ring modulator. **a,** Three-dimensional sketch of the device. Insets show the detailed top and cross-sectional views at the modulation section. The structural parameters for the electrode are (r, c, s, t, h, g, w_s, d_1, d_2, h_w, h_l, h_r) = (47, 3, 2, 5, 15, 1.8, 75, 1.1, 0.2, 9, 39, 35) μm. **b,** Microscope picture of a finished device. **c,d,** Scan electron microscope pictures of the directional coupler and the CLTW electrode, respectively. **e,f,** Working principle of the coupling modulation when the device is at the critical-coupled state and the zero-coupled state, respectively.

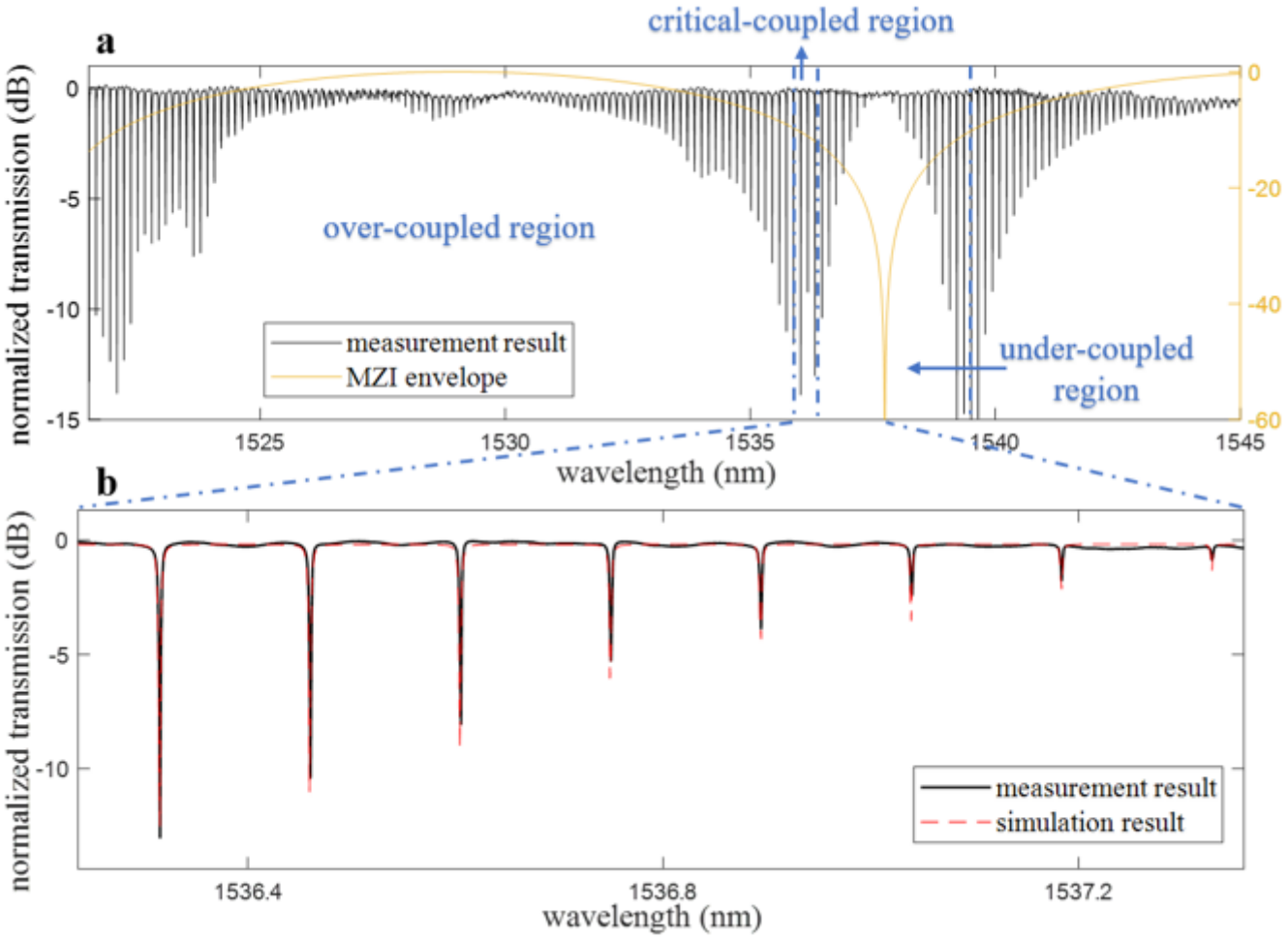

Figure 2

Transmission spectra of the device. a, Wide wavelength scan showing a composited the MZI and ring response. The simulated cross-port coupling spectrum of the MZI is also plotted. **b**, Zoom-in view of the spectrum at the under-coupled region. The work wavelengths of the device should be selected at the resonances of the ring.

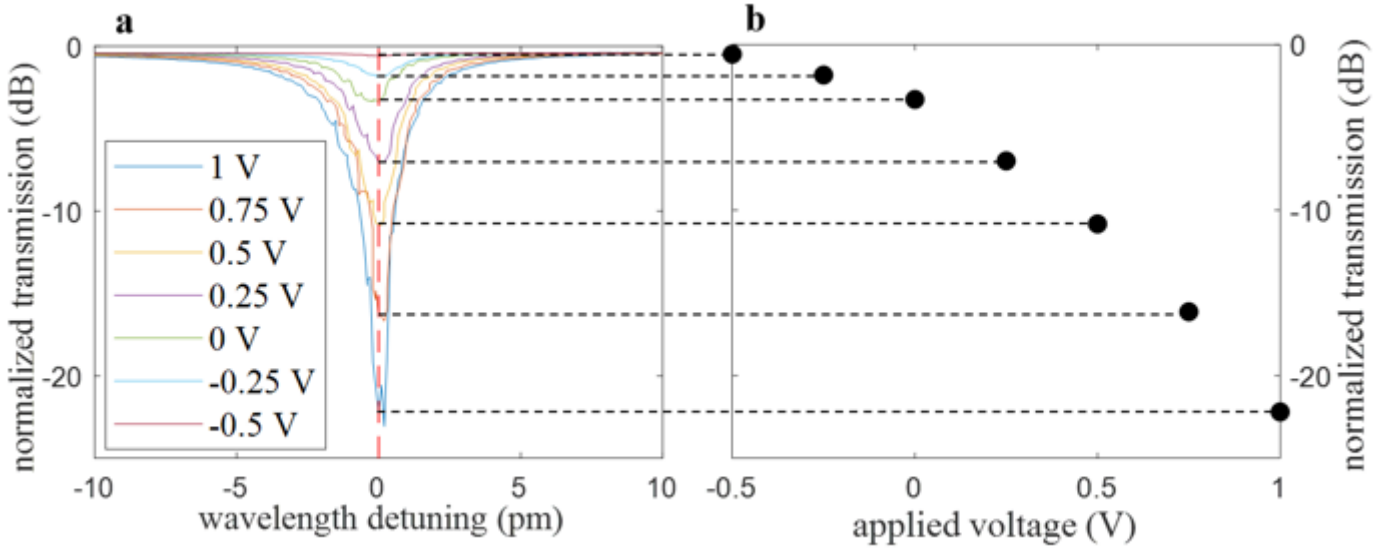

Figure 3

DC voltage response of the device. **a**, Recorded transmission spectra around one resonant wavelength of 1536.8943nm when the applied DC voltages changed from 1 V to -0.5 V. **b**, Corresponding transmission at 1536.8943nm as a function of applied DC voltages where the experimental data are shown in black dots, and the red line is a linear fit.

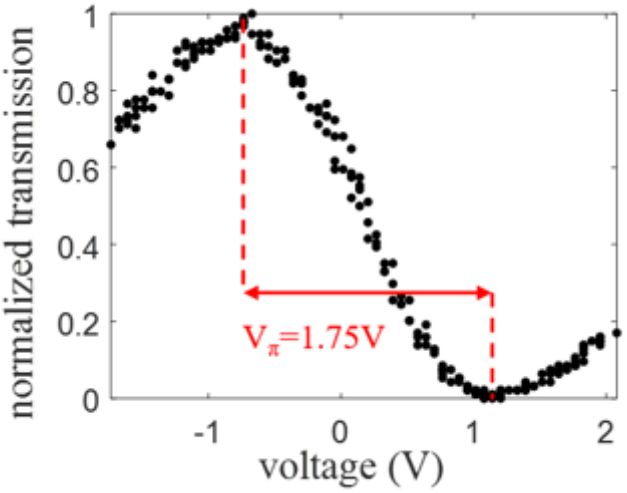

Figure 4

***V_p* measurement for the device.** Normalized optical transmission as a function of applied voltages under a triangular-wave scan at 100 kHz.

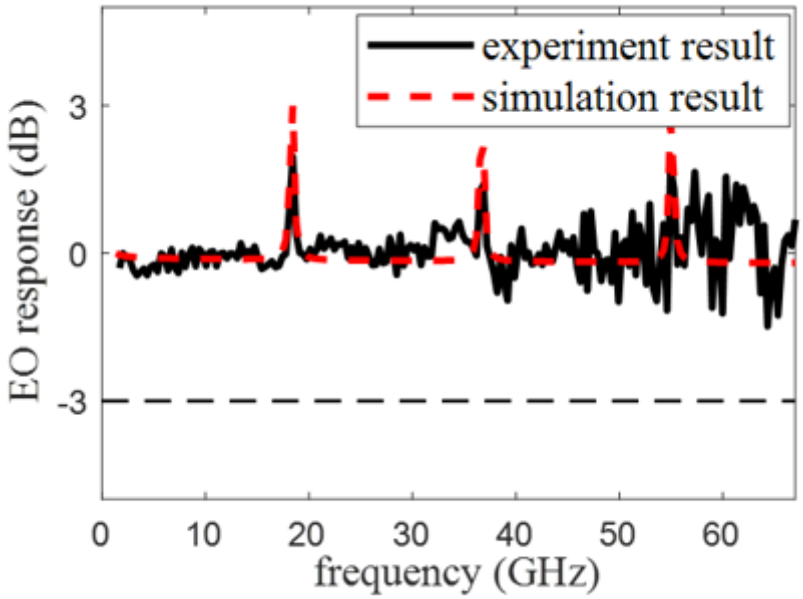

Figure 5

EO frequency responses of the device. The EO response of the device was measured at the wavelength of 1536.8943 nm until 67 GHz. The simulation result is discussed in Supplementary Note 3.

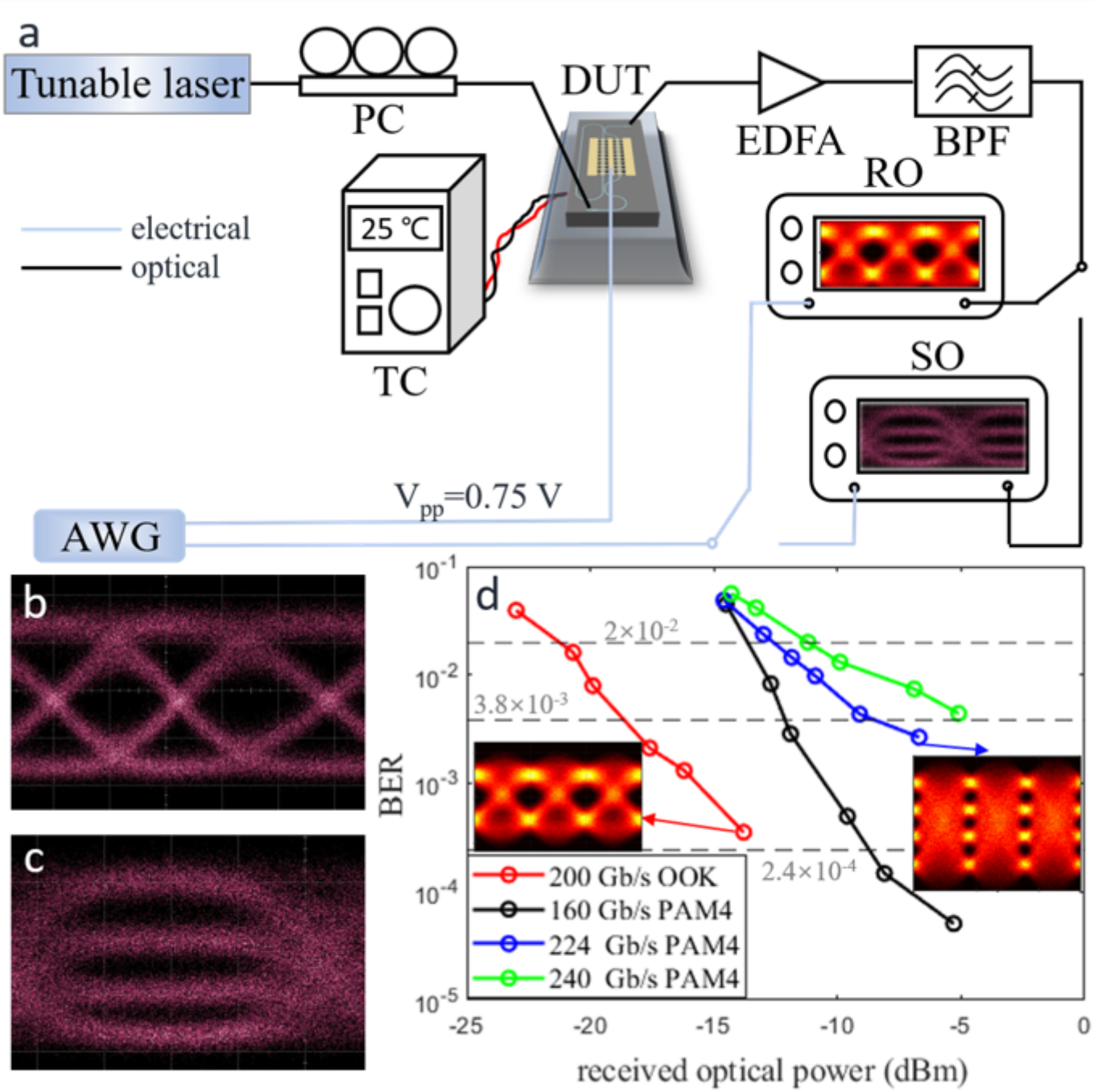

Figure 6

High-speed data transmission performance of the device. a, Experimental setup for measuring the eye diagrams and the BERs. **b**, Transmitted eye diagram for an OOK signal at a data rate of 160 Gb/s. **c**, Transmitted eye diagram for a PAM-4 signal at a data rate of 40 Gbaud (80 Gb/s). **d,** BERs of the transmitted 200 Gb/s OOK, 160 Gb/s PAM-4, 224 Gb/s PAM-4, and 240 Gb/s PAM-4 signals with different received optical powers. The insets show the calculated eye diagrams after DSP for the 200 Gb/s OOK and 224 Gb/s PAM-4 signals. The peak-to-peak driving voltages for all the above measurement were 0.75 V.

Supplementary Files

This is a list of supplementary files associated with this preprint. Click to download.

- SupplementaryInformation5.docx